ELSEVIER

Comput. Methods Appl. Mech. Engrg. 190 (2001) 5391–5412

Computer methods in applied mechanics and engineering

www.elsevier.com/locate/cma

An adaptive finite element method for viscoplastic fluid flows in pipes

Pierre Saramito *, Nicolas Roquet

LMC-IMAG, B.P. 53, 38041 Grenoble Cedex 9, France

Received 2 June 2000

Abstract

The numerical modelling of the fully developed Poiseuille flow of a yield stress fluid in a square section is presented. The dead regions in outer corners and the plug region in the center are exhibited. Numerical computations cover the complete range of the dimensionless number describing the yield stress effect, from a Newtonian flow to a fully stopped flow. The resolution of variational inequalities describing the flow is based on the augmented Lagrangian method and a specific mixed finite element method. The localization of yield surfaces is approximated by an anisotropic auto-adaptive mesh procedure. The limit load analysis and the associated limit yield surface are obtained by an extrapolation procedure. © 2001 Elsevier Science B.V. All rights reserved.

Keywords: Yield stress fluids; Bingham model; Variational inequalities; Limit load analysis; Adaptive mesh; Mixed finite element methods

1. Introduction

One of the difficult problems in viscoplastic fluid mechanics is to predict the appearance and development of dead regions with the variation of material properties and flow parameters. Understanding yield stress mechanisms is of major importance in petroleum industry (pipe-line), food industry, ceramics extrusion, bricks, debris flows, and semi-solid materials. Furthermore, the characteristics of dead regions and flow curves are of particular interest in the design of extrusion geometries.

The fully developed flow of a Bingham fluid in a tube with a square cross-section (see Fig. 1(a)), contains most of the features of viscoplastic flows. In a *plug region*, located in the center of the section (see Fig. 1(b)), the material translates with a constant velocity, while four *dead regions* are located in the outer corners. In contrast, the flow in a circular tube does not exhibit dead regions. Plug and dead regions are characterized by a rigid body motion of the material, and are related to *rigid zones*, by contrast to *shear zones*, where the material deforms. The separation surfaces between rigid and shear zones are related to the *yield surfaces*.

By using variational methods, Mosolov and Mjasnikov [1] showed the existence and uniqueness of the plug region. The existence of dead regions and the fact that dead regions always present a concavity turned towards the inside of the section is also showed in [2]. Accurate exhibition of such flow patterns represents a challenge for numerical methods.

The pour accuracy of most numerical simulations can be explained in part by the replacement of the viscoplastic model by more regular ones, such as non-linear biviscous laws (see [3–5]). These biviscous laws introduce an additional regularization parameter. The practical difficulty to solve the regularized model

* Corresponding author. Tel.: +33-4-76-51-46-10; fax: +33-4-76-63-12-63.
E-mail address: pierre.saramito@imag.fr (P. Saramito).

0045-7825/01/$ - see front matter © 2001 Elsevier Science B.V. All rights reserved.
PII: S0045-7825(01)00175-X

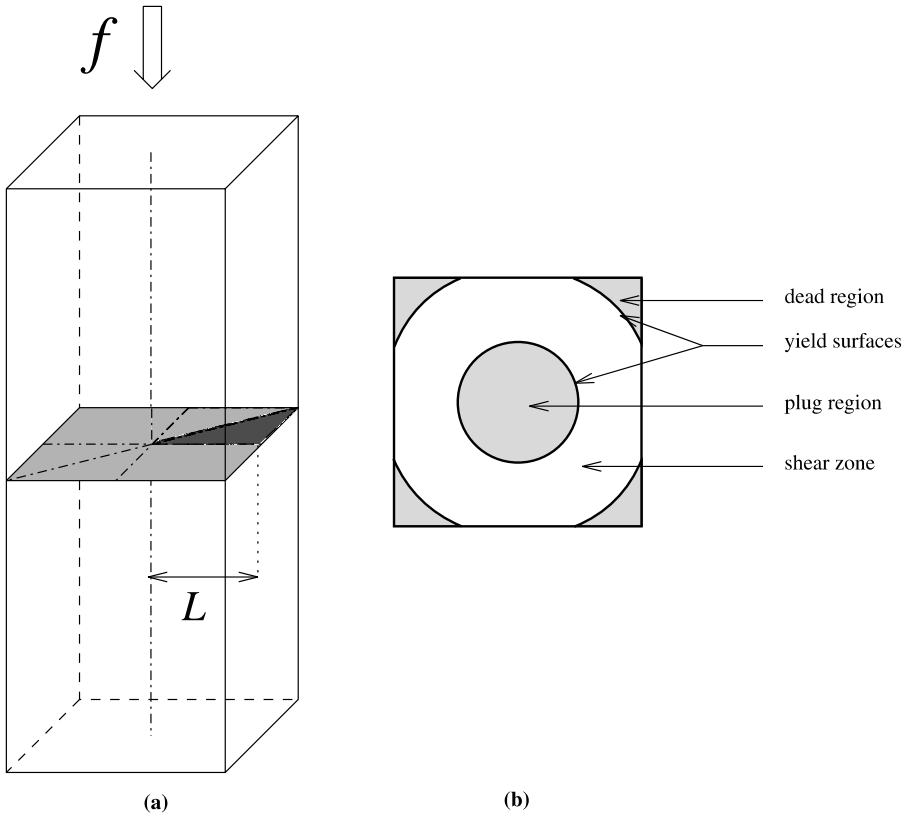

Fig. 1. Square tube cross-section: (a) tri-dimensional view; (b) schematic view of the cross-section.

problem increases when the regularization parameter approaches zero, i.e., when the regularized model approaches the less regular viscoplastic model. Furthermore, the computational time grows very rapidly when the regularization parameter approaches zero. Finally, all rigid zones disappear completely as soon as the regularized model is used, and the notion of zones with *small deformations* may be introduced. As a consequence, regularized model studies encounter difficulties to provide accurate solutions, especially in the most interesting case where yield properties become important. Nevertheless, biviscosity models are widely used, since most available numerical codes for solving Newtonian flows with a non-constant viscosity function can directly be re-used. Recently, Taylor and Wilson [6] explored the resolution of the Bercovier and Engelman [3] regularized model in square and rectangular tube sections. These authors exhibited some dead regions. Nevertheless, unexpected situations were exhibited: the concavity of the dead regions were inverted, and dead and plug regions was connected. The dramatic effect of the regularization parameter on the inversion of concavity has been analyzed by Wang [7]. The author showed that these unexpected effects were caused by an insufficient accuracy of the numerical simulation.

The replacement of the Bingham model by regularized one can be avoided in practical computations: in the framework of variational inequalities, Fortin [8] proposed an algorithm to solve the flow of a Bingham fluid in a square cross-section. Moreover, the author exhibited results for the flow in a square section. Nevertheless, meshes were rough, and a dead region was represented by only one triangular element. The augmented Lagrangian framework introduced by Fortin and Glowinski [9], later developed by Glowinski and LeTallec [10], has furnished efficient algorithms for solving viscoplastic flow problems. Since this approach does not require the use of a regularized model, an accurate prediction of rigid zones could be expected. Huilgol and Panizza [11] applied this approach to the resolution of a Bingham model in a L-shaped tube section. A plug region was found at the center of the section. Nevertheless, as pointed out by Wang [12], the flow field in the corner regions was not clearly resolved by these authors.

Even when using augmented Lagrangian method for solving the exact Bingham model, the finite element prediction of the yield surface is not accurate enough. The first improvement is to increase the polynomial degree used by the finite element method. The second improvement is to increase mesh refinement. A uniform mesh refinement increases the computational time rapidly, while the accuracy increases slowly in terms of the yield surface determination. The idea of anisotropic auto-adaptive mesh generation, introduced in 1990 by Vallet [13] and developed by Borouchaki et al. [14] has been recently used for the simulation of Euler and Navier–Stokes equation by Castro-Diaz et al. [15] to capture shocks accurately, i.e. surfaces where the solution is discontinuous. By analogy, in the context of viscoplastic flows, the second derivatives of the velocity field are generally discontinuous across yield surfaces. Since such surfaces are a priori unknown, mesh refinement requires an iterative process to catch the solution and obtain a high precision for yield surfaces.

In this paper, the flow of a Bingham fluid along a pipe of square cross-section is considered. The numerical technique combines the augmented Lagrangian method that takes rigorously into account the yield stress constitutive equation, and the auto-adaptive mesh procedure for the capture of surfaces associated with abrupt variations of the solution.

The second section presents the Bingham model and states the problem of the flow along a prismatic tube. Numerical methods and tests are grouped in the third section. The augmented Lagrangian algorithm is recalled. Then, the stress-and-velocity mixed finite element approximation is introduced. The validation uses a circular tube section. The efficiency of the mesh adaptation strategy is tested on both circular and cross-square sections. The fourth section presents results on a square cross-section, including rigid zone enhancement and velocity and stress profiles. The limit case where rigid zones invade the whole section, related to the *limit load analysis*, is treated using an extrapolation procedure. Finally, a scaling procedure extends the flow curve of a circular pipe to the case of the squared pipe. Two short appendixes group explicit expressions of some constants.

2. Problem statement

The Bingham model [16,17] is characterized by the following property: the material starts to flow only if the applied forces exceed a certain limit σ_0, called the yield limit. The total Cauchy stress tensor is expressed by

$$\sigma_{\text{tot}} = -p \cdot I + \sigma,$$

where σ denotes its deviatoric part, and p is the pressure. The conservation of momentum is

$$\rho\left(\frac{\partial \mathbf{u}}{\partial t} + \mathbf{u} \cdot \nabla \mathbf{u}\right) - \mathbf{div}\ \sigma + \nabla p = 0,$$

where $\mathbf{u}$ is the velocity field, and ρ the constant density. Since the fluid is assumed to be incompressible, the mass conservation leads to

$$\text{div}\ \mathbf{u} = 0.$$

The constitutive equation can be written as:

$$\sigma = 2\eta D(\mathbf{u}) + \sigma_0 \frac{D(\mathbf{u})}{|D(\mathbf{u})|} \quad \text{if } |D(\mathbf{u})| \neq 0,$$
$$|\sigma| \leqslant \sigma_0 \quad \text{if } |D(\mathbf{u})| = 0,$$

or equivalently:

$$D(\mathbf{u}) = \begin{cases} \left(1 - \frac{\sigma_0}{|\sigma|}\right)\frac{\sigma}{2\eta} & \text{if } |\sigma| > \sigma_0, \\ 0 & \text{otherwise,} \end{cases}$$

where $\sigma_0 \geqslant 0$ is the yield stress, $\eta > 0$ is the plastic viscosity, $D(\mathbf{u}) = (\nabla\mathbf{u} + \nabla\mathbf{u}^{\mathrm{T}})/2$ is the rate-of-deformation tensor, and, for any tensor $\tau = (\tau_{ij})$, the notation $|\tau|$ represents the following matrix norm:

$$|\tau| = \sqrt{\frac{\tau : \tau}{2}} = \frac{1}{\sqrt{2}} \left(\sum_{ij} \tau_{ij}^2 \right)^{1/2}.$$

Notice that $\sigma_0 = 0$, one is led to the classical viscous incompressible fluid. When $\sigma_0 > 0$, rigid zones in the interior of the fluid can be observed. As σ_0 becomes larger, these rigid zones develop and may completely block the flow when σ_0 is sufficiently large.

We consider the fully developed flow in a prismatic tube (see Fig. 1(a)). Let (O_z) be the axis of the tube and (O_{xy}) the plane of the bounded section $\Omega \subset \mathbb{R}^2$. The pressure gradient is written as $\nabla p = (0, 0, -f)$ in Ω, where $f > 0$ is the constant applied force density. The velocity is written as $\mathbf{u} = (0, 0, u)$, where the third component u along the (O_z) axis depends only upon x and y, and is independent of t and z. The problem can be considered as a two-dimensional one, and the stress tensor σ is equivalent to a two shear stress component vector: $\boldsymbol{\sigma} = (\sigma_{xz}, \sigma_{yz})$. We also use the following notations:

$$\nabla u = \left(\frac{\partial u}{\partial x}, \frac{\partial u}{\partial y} \right),$$
$$\operatorname{div} \boldsymbol{\sigma} = \frac{\partial \sigma_{xz}}{\partial x} + \frac{\partial \sigma_{yz}}{\partial y},$$
$$|\boldsymbol{\sigma}| = \sqrt{\sigma_{xz}^2 + \sigma_{yz}^2}.$$

Finally, the so-called Mosolov problem can be summarized as:

(P): find $\boldsymbol{\sigma}$ and u defined in Ω such that

$$\nabla u = \begin{cases} \left(1 - \frac{\sigma_0}{|\boldsymbol{\sigma}|}\right) \frac{\boldsymbol{\sigma}}{\eta} & \text{if } |\boldsymbol{\sigma}| > \sigma_0, \\ 0 & \text{otherwise}, \end{cases} \tag{1}$$

$$\operatorname{div} \boldsymbol{\sigma} = -f \text{ in } \Omega, \tag{2}$$

$$u = 0 \text{ on } \partial\Omega. \tag{3}$$

Here, (1) expresses the constitutive equation, (2) the conservation of momentum and (3) the no-slip boundary condition. In the case of a square cross-section, we reduce the domain of computation by using symmetries (see Fig. 1(a)). Thus, in this paper, results for the square cross-section are represented in a triangular domain.

Let L be a characteristic length of the cross-section Ω, i.e., the half-length of an edge of a square section, or the radius of a circular section (also denoted by R for convenience in that case). A characteristic velocity is given by $U = L^2 f/(2\eta)$ and a characteristic viscous stress by $\Sigma = \eta U/L = Lf/2$. The Bingham dimensionless number is defined by the ratio of the yield limit σ_0 by a representative viscous stress Σ

$$Bi = \frac{2\sigma_0}{Lf}. \tag{4}$$

This is the only dimensionless number of the problem.

3. Numerical methods and tests

The augmented Lagrangian method, applied to the Mosolov problem (1)–(3), is briefly introduced in this appendix. Then, the delicate problem of the choice of a mixed finite element is carefully treated. Next, the validation of our numerical methodology on a circular pipe with uniform meshes is presented. Finally, our mesh adaptation strategy is tested and discussed.

3.1. Augmented Lagrangian algorithm

Let $H_0^1(\Omega)$ denote the classical functional space [18] and J the functional defined for all $v \in H_0^1(\Omega)$ by

$$J(v) = \frac{\eta}{2}\int_\Omega |\nabla v|^2 \,\mathrm{d}x + \sigma_0 \int_\Omega |\nabla v| \,\mathrm{d}x - \int_\Omega fv \,\mathrm{d}x.$$

Glowinski et al. [19] showed that the solution u of problem (P) expressed as a minimization point of J on $H_0^1(\Omega)$

$$\min_{v\in H_0^1(\Omega)} J(v). \tag{5}$$

Since J is non-differentiable on $H_0^1(\Omega)$ when $\sigma_0 > 0$ due to the term $\int_\Omega |\nabla v| \mathrm{d}x$, the problem cannot be described by an equation and thus requires a specific convex optimization approach (see also [20]).

Let

$$\boldsymbol{\gamma} = \nabla u \in L^2(\Omega)^2. \tag{6}$$

The linear constraint (6) is handled by using a Lagrange multiplier that coincides with the stress $\boldsymbol{\sigma} \in L^2(\Omega)^2$

$$\mathscr{L}(u, \boldsymbol{\gamma}; \boldsymbol{\sigma}) = \frac{\eta}{2}\int_\Omega |\boldsymbol{\gamma}|^2 \,\mathrm{d}x + \sigma_0 \int_\Omega |\boldsymbol{\gamma}| \,\mathrm{d}x - \int_\Omega fv \,\mathrm{d}x + \int_\Omega (\nabla u - \boldsymbol{\gamma}) \cdot \boldsymbol{\sigma} \,\mathrm{d}x.$$

For all $a > 0$, the augmented Lagrangian

$$\mathscr{L}_a(u, \boldsymbol{\gamma}; \boldsymbol{\sigma}) = \mathscr{L}(u, \boldsymbol{\gamma}; \boldsymbol{\sigma}) + \frac{a}{2}\int_\Omega \nabla u - \boldsymbol{\gamma}|^2 \,\mathrm{d}x$$

becomes quadratic and positive-definite with respect to u. This implies that, with $\boldsymbol{\sigma}$ and $\boldsymbol{\gamma}$ fixed, $\mathscr{L}_a$ can be minimized with respect to u on $H_0^1(\Omega)$, whereas this operation becomes in practice impossible for $a = 0$. This transformation becomes helpful since we can solve the saddle-point problem of $\mathscr{L}_a$, that coincides with those of $\mathscr{L}$, by an appropriate algorithm proposed in [9]:

Algorithm (Uzawa)

initialization: $n = 0$

Let $\boldsymbol{\sigma}^0$ and $\boldsymbol{\gamma}^0$ arbitrarily chosen in $L^2(\Omega)^2$.

loop: $n \geqslant 0$

- *Step 1*: Let $\boldsymbol{\sigma}^n$ and $\boldsymbol{\gamma}^n$ being known, find $u^{n+1} \in H_0^1(\Omega)$ such that

$$-a\Delta u^{n+1} = f + \operatorname{div}(\boldsymbol{\sigma}^n - a\boldsymbol{\gamma}^n) \text{ in } \Omega, \tag{7}$$

$$u^{n+1} = 0 \text{ on } \partial\Omega. \tag{8}$$

- *Step 2*: compute explicitly:

$$\boldsymbol{\gamma}^{n+1} := \begin{cases} \left(1 - \frac{\sigma_0}{|\boldsymbol{\sigma}^n + a\nabla u^{n+1}|}\right)\frac{\boldsymbol{\sigma}^n + a\nabla u^{n+1}}{\eta + a} & \text{if } |\boldsymbol{\sigma}^n + a\nabla u^{n+1}| > \sigma_0, \\ 0 & \text{otherwise .} \end{cases} \tag{9}$$

- *Step 3*: compute explicitly:

$$\boldsymbol{\sigma}^{n+1} := \boldsymbol{\sigma}^n + a(\nabla u^{n+1} - \boldsymbol{\gamma}^{n+1}). \tag{10}$$

end loop

The interest of this algorithm is that it transforms the global non-differentiable problems (5) into a family of completely standard problem (7), (8) and local explicit computation (9), coordinated via the Lagrange multiplier in (10).

3.2. Stress–velocity mixed finite element approximation

Let A and B be the two bilinear forms defined by

$$A(\gamma,u;\xi,v)=(\eta+a)\int_\Omega \gamma\cdot\xi\,\mathrm{d}x-a\int_\Omega \nabla u\cdot\xi\,\mathrm{d}x-a\int_\Omega \nabla v\cdot\gamma\,\mathrm{d}x+a\int_\Omega \nabla u\cdot\nabla v\,\mathrm{d}x,$$

$$B(\xi,v;\tau)=-\int_\Omega \xi\cdot\tau\,\mathrm{d}x+\int_\Omega \nabla v\cdot\tau\,\mathrm{d}x.$$

The saddle point of $\mathscr{L}_a$ is characterized as the solution of a problem expressed by the following variational inequalities:

(FV): find $(\gamma,u;\sigma)\in L^2(\Omega)^2\times H_0^1(\Omega)\times L^2(\Omega)^2$ such that

$$\sigma_0\int_\Omega(|\xi|-|\gamma|)\,\mathrm{d}x+A(\gamma,u;\xi-\gamma,v)+B(\xi-\gamma,v;\sigma)\geqslant\int_\Omega fv\,\mathrm{d}x,$$

$$B(\gamma,u;\tau)=0$$

for all $(\xi,v;\tau)\in L^2(\Omega)^2\times H_0^1(\Omega)\times L^2(\Omega)^2$.

Let $D_h\subset L^2(\Omega)$, $V_h\subset H_0^1(\Omega)$, and $T_h\subset L^2(\Omega)$ be some finite dimensional spaces. The finite dimensional version of the variational inequalities is simply obtained by replacing functional spaces by their finite dimensional counterparts:

(FV)$_h$: find $(\gamma_h,u_h;\sigma_h)\in D_h\times V_h\times T_h$ such that

$$\sigma_0\int_\Omega(|\xi|-|\gamma_h|)\,\mathrm{d}x+A(\gamma_h,u_h;\xi-\gamma_h,v)+B(\xi-\gamma_h,v;\sigma)\geqslant\int_\Omega fv\,\mathrm{d}x,$$

$$B(\gamma_h,u_h;\tau)=0$$

for all $(\xi,v;\tau)\in D_h\times V_h\times T_h$.

For $\sigma_0=0$ the problem reduces to a linear one that fits the theory of mixed finite elements (see, e.g., [21]). The choice $D_h=T_h$ leads to $\gamma_h=R_h\nabla u_h$, where R_h denotes the projection from $L^2(\Omega)^2$ on T_h, defined for all $\xi\in L^2(\Omega)^2$ by:

$$R_h\xi\in T_h \text{ and } \int_\Omega R_h\xi\cdot\tau\,\mathrm{d}x=\int_\Omega\xi\cdot\tau\,\mathrm{d}x\quad\forall\tau\in T_h.$$

See also [22] for the use of the properties of R_h in the context of stabilized mixed finite element approximation. An investigation of stress–velocity mixed finite element space combinations that satisfies $R_h=I$ is

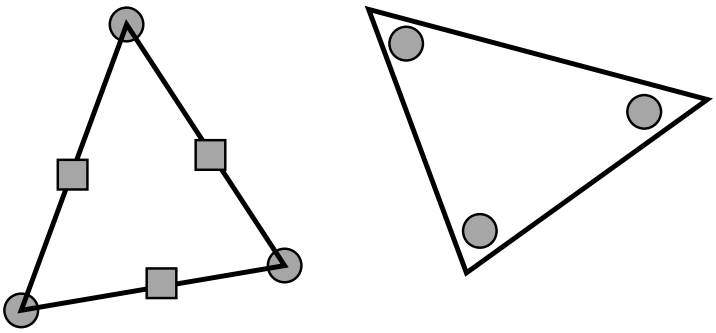

Fig. 2. Mixed finite element approximation.

presented in [23] and applied in the context of viscoelastic fluid flows [24]. Thus, the case $\sigma_0 = 0$ leads to $\boldsymbol{\sigma}_h = \eta R_h \nabla u_h$ and the problem reduces to the following linear elliptic one:

$(Q)_h$: find $u_h \in V_h$ such that

$$\eta \int_\Omega R_h \nabla u_h \cdot R_h \nabla v \, \mathrm{d}x + a \int_\Omega (I - R_h) \nabla u_h \cdot (I - R_h) \nabla v \, \mathrm{d}x = \int_\Omega f v \, \mathrm{d}x \quad \forall v \in V_h.$$

When $R_h \neq I$ i.e. $T_h \neq \nabla V_h$, the discrete solution u_h depends upon the numerical parameter $a > 0$ of the augmented Lagrangian method. This property is not desirable. A necessary and sufficient condition for the solution u_h to be independent of the parameter a is $T_h = \nabla V_h$.

Let $\mathscr{T}_h$ be a finite element mesh composed of triangles. We introduce the space V_h, composed of continuous piecewise polynomial quadratic functions ($P_2 - C^0$). Thus, $T_h = D_h = \nabla V_h$ is the set of discontinuous piecewise linear functions ($P_1 - C^{-1}$). Fig. 2 represents the corresponding degrees of freedom. In a preliminary version, the space V_h was implemented by continuous piecewise linear functions ($P_1 - C^0$), and $T_h = D_h$ by discontinuous piecewise constant functions ($P_0 - C^{-1}$). The quadratic implementation leads to a better approximation, and thus, is well-suited to exhibit fine flow patterns.

3.3. Validation on a circular tube

This subsection presents the validation of the numerical methodology on a circular pipe, since the analytical solution is known. Let Ω be a section of a circular pipe of radius R and center $(x, y) = (0, 0)$. Let $r = \sqrt{x^2 + y^2}$ for convenience. The Bingham number is defined by $Bi = 2\sigma_0/(fR)$. For $2\sigma_0 \geqslant fR$, i.e. $Bi \geqslant 1$, the flow is completely blocked and the velocity field is zero. When $2\sigma_0 < fR$, the velocity field $u(r)$ is given by:

$$\frac{2\eta}{fR^2} \times u(r) = \begin{cases} \frac{1}{2}\left(1 - \frac{r^2}{R^2}\right) - \frac{2\sigma_0}{fR}\left(1 - \frac{r}{R}\right) & \text{when } \frac{r}{R} \geqslant \frac{2\sigma_0}{fR}, \\ \frac{1}{2}\left(1 - \frac{2\sigma_0}{fR}\right)^2 & \text{otherwise .} \end{cases}$$

Thus, a plug flow of radius $2\sigma_0/f$ exists, which translates at constant velocity in the (O_z) direction. Note that the solution $u(r)$ is only one time differentiable, since the gradient of velocity is non-differentiable at the junction between the shear and the plug zones (i.e. at $r = 2\sigma_0/f$).

Fig. 3 shows the evolution of the normalized residual term $\|\boldsymbol{\gamma}_h^n - \nabla u_h^n\|_{L^2(\Omega)}$ versus the iteration number n for three values of the numerical parameter a of the algorithm. Note that $a = 20$ leads to an optimal convergence velocity. For $n \approx 1400$, the computation reaches the machine precision, roughly 10^{-30} in quadruple precision. For $a = 5$ or $a = 50$, the convergence is slower. Recall that the limit u_h of the family $(u_h^n)_{n \geqslant 0}$ does not depend upon a, since the finite element approximation for velocity and stresses are carefully chosen. Note also on Fig. 3 the asymptotic slope on the semi-logarithmic scale. This slope is related to the convergence velocity v^* defined by

$$v^* = \lim_{n \to \infty} -\frac{1}{n} \log \|\boldsymbol{\gamma}_h^n - \nabla u_h^n\|_{L^2(\Omega)}.$$

Fig. 4 shows v^* versus a for various uniform mesh size h and Bingham number. Fig. 5 presents a family of three uniform finite element meshes with decreasing element size h. We observe that the optimal convergence velocity occurs for a value of a that depends upon h and Bi. The optimal a increases when $h \to 0$ and Bi increases, while the corresponding optimal convergence velocity v^* decreases. This expresses that the computation time increases with mesh size and Bi. From a practical point of view, the optimal value of a is difficult to predict, since it depends strongly upon the dimensionless number Bi, and the finite element mesh. Nevertheless, the algorithm converges for all $a > 0$. For all computations of the previous section, involving adaptive meshes, the value $a = 200$ has been used, and iterations were performed until the maximum of $|\boldsymbol{\gamma}_h^n - \nabla u_h^n|$ over Ω becomes lower than 10^{-12}.

Let us turn to the convergence of u_h versus the mesh size $h \to 0$ for the uniform mesh family. The exact solution u is known for the circular pipe and Fig. 6 plots in logarithmic scale the error in L^2-norm versus h.

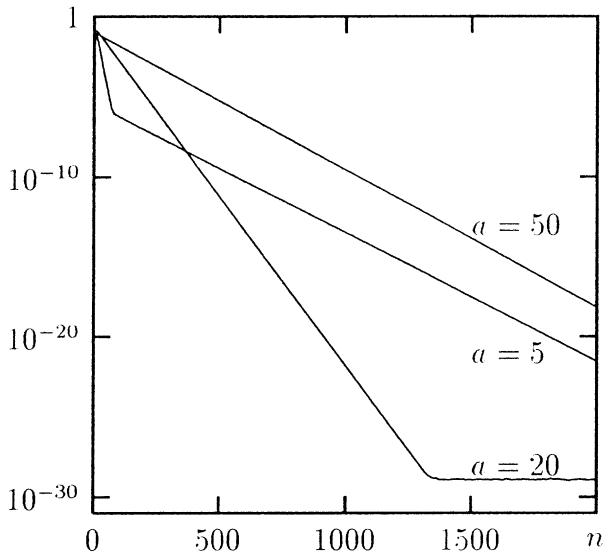

Fig. 3. Normalized residual terms $\|\gamma_h^n - \nabla u_h^n\|_{L^2(\Omega)} / \|\gamma_h^0 - \nabla u_h^0\|_{L^2(\Omega)}$ versus algorithm iteration number n.

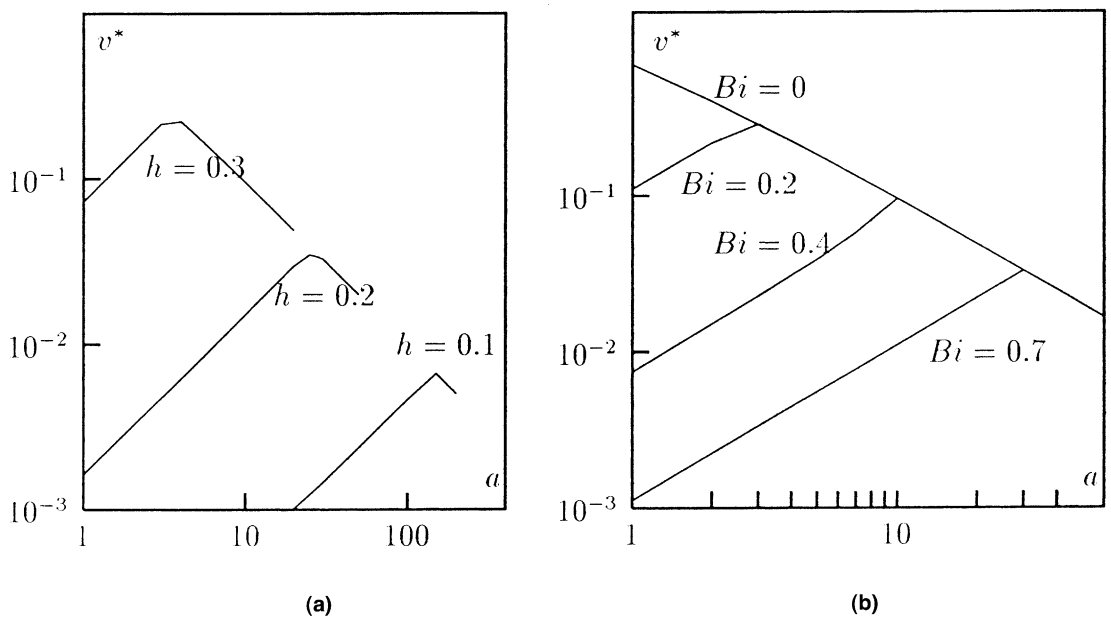

Fig. 4. Algorithm convergence velocity v^* versus a: (a) varying mesh size and for $Bi = 0.5$; (b) varying Bi and for mesh size $h = 0.2$.

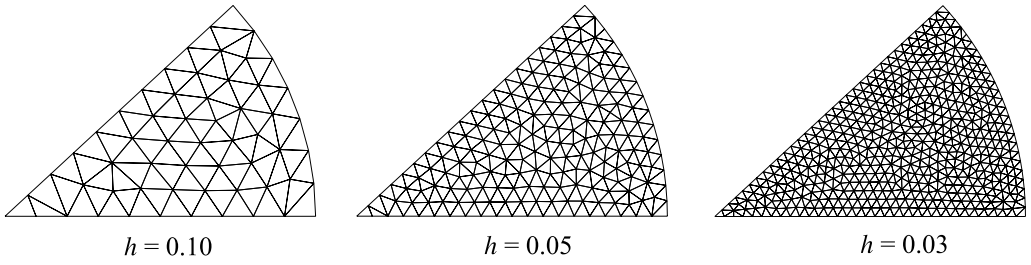

Fig. 5. The uniform mesh family used for the convergence validation.

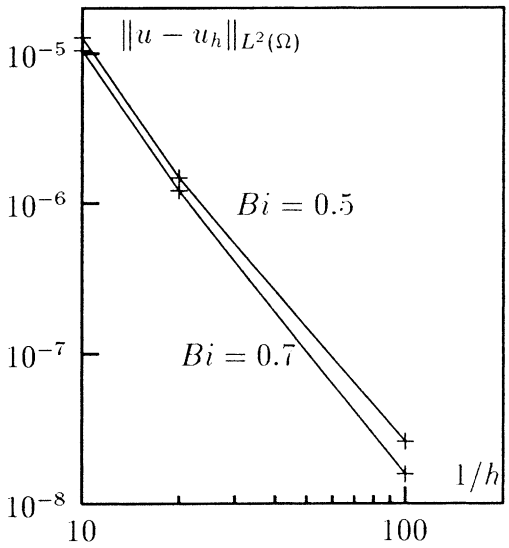

Fig. 6. Convergence of the finite element method: $\|u - u_h\|_{L^2(\Omega)}$ as a function of the mesh size h.

Observe that the error decreases rapidly with h. The error is about 10^{-8} for $h = 10^{-2}$. More generally, the error behaves as $\mathcal{O}(h^\lambda)$, where λ is in the range 2–3. The continuous P_2 finite element, used for the velocity, is responsible of this efficient convergence property. In the case of the continuous P_1 element, the convergence is slower: Glowinski [25] showed a $\mathcal{O}(h\sqrt{|\ln(h)|})$ behavior for the error in H^1-norm, and Falk and Mercier [26] showed an optimal $\mathcal{O}(h)$ estimate for the vorticity in L^2-norm when Ω is connected. When using the P_2 element, Roquet et al. [27] showed recently a $\mathcal{O}(h^2\sqrt{|\ln(h)|})$ estimate for the velocity in H^1-norm.

Finally, let us introduce the field of dissipative energy, defined in Ω by

$$E = \eta|\nabla u|^2 + \sigma_0|\nabla u|.$$

This field E is known to be non-differentiable across the border between shear and rigid zones, as can be seen with its explicit expression:

$$\frac{4\eta}{f^2R^2} \times E(r) = \begin{cases} \left(\frac{r}{R}\right)^2 - \frac{2\sigma_0}{fR} \times \frac{r}{R} & \text{when } \frac{r}{R} \geqslant \frac{2\sigma_0}{fR}, \\ 0 & \text{otherwise.} \end{cases} \tag{11}$$

Notice that E is continuous, but its first derivative is discontinuous. The following subsection, related to the mesh adaptation process, exploits this important property.

3.4. Mesh adaptation

Let $\mathcal{T}_0$ be an initial mesh and u_0 be the solution of problem $(\mathrm{FV})_h$ associated to $\mathcal{T}_0$. Next, let $\varphi_0 = \varphi(u_0)$ be the *governing field* obtained from ∇u_0 by

$$\varphi_0 = \left(\eta|\nabla u_0|^2 + \sigma_0|\nabla u_0|\right)^{1/2}.$$

Note that φ_0 is the square root of the dissipative energy. This choice will be explained in the following subsection. The governing field φ_0 is approximated by a piecewise polynomial function over each triangle $K \in \mathcal{T}_0$, and the error of interpolation in the unitary direction $\mathbf{d} \in \mathbb{R}^2$ is estimated by:

$$e_{K,\mathbf{d}} = h_{K,\mathbf{d}}^2 \left| \frac{\partial^2 \varphi_0}{\partial \mathbf{d}^2} \right| \quad \text{in } K,$$

where $h_{K,\mathbf{d}}$ is the length of K in the $\mathbf{d}$ direction,

$$\frac{\partial^2\varphi_0}{\partial\mathbf{d}^2} = \mathbf{d}^{\mathrm{T}} \cdot H(\varphi_0) \cdot \mathbf{d}$$

and $H(\varphi_0)$ denotes the Hessian of φ_0

$$H(\varphi_0) = \begin{pmatrix} \partial^2\varphi_0/\partial x^2 & \partial^2\varphi_0/\partial x\partial y \\ \partial^2\varphi_0/\partial x\partial y & \partial^2\varphi_0/\partial y^2 \end{pmatrix}.$$

Following Vallet [13], a possibility to adapt the mesh to the computation of φ_0 is to equi-distribute this error, i.e. to make it constant over all triangles and in all directions. Let λ_1, λ_2 be the eigenvalues of $H(\varphi_0)$ and $\mathbf{d}_1$ and $\mathbf{d}_2$ the associated eigenvectors:

$$\frac{\partial^2\varphi_0}{\partial\mathbf{d}_1^2} = \lambda_1 \quad \text{and} \quad \frac{\partial^2\varphi_0}{\partial\mathbf{d}_2^2} = \lambda_2.$$

The error $e_{K,\mathbf{d}}$ is independent of $\mathbf{d}$ and K when $e_{K,\mathbf{d}_1} = e_{K,\mathbf{d}_2}$, i.e. when

$$h_{K,\mathbf{d}_1}^2|\lambda_1| = h_{K,\mathbf{d}_2}^2|\lambda_2| = c_0 \quad \forall K \in \mathscr{T}_0,$$

where $c_0 > 0$ is a constant independent of K. The Hessian $H(\varphi_0)$ being known over K, we suppose that $H(\varphi_0)$ is non-singular, i.e. $\lambda_1\lambda_2 \neq 0$. The constant c_0 being known, we want to build triangles of length h_i in the $\mathbf{d}_i$ direction with $h_i = \sqrt{c_0/|\lambda_i|}$, $i = 1, 2$. Such a triangle has no privileged direction in a metric such that the two $h_i\mathbf{d}_i$ vectors, $i = 1, 2$, have the same norm. Thus, we introduce the metric $M(\varphi_0)$, the eigenvectors as column of $H(\varphi_0)$ with the corresponding $|\lambda_1|$ and $|\lambda_2|$. The induced norm $\|\cdot\|_M$ satisfies

$$\|h_i\mathbf{d}_i\|_M = h_K\sqrt{\mathbf{d}_i^T \cdot M(\varphi_0) \cdot \mathbf{d}_i} = \sqrt{c_0}, \quad k = 1, 2.$$

Thus, an isotropic mesh in the Riemann space associated to the metric $M(\varphi_0)$ is a mesh extended in the Euclidean space with a factor h_i in the $\mathbf{d}_i$ direction.

Solving a problem using a mesh adaptation is an iterative process, which involves three main steps:

1. Starting from an initial mesh $\mathscr{T}_0$, the problem is solved using the augmented Lagrangian algorithm. Let u_0 be the corresponding solution associated to the mesh $\mathscr{T}_0$.
2. Let $\varphi_0 = (\eta|\nabla u_0|^2 + \sigma_0|\nabla u_0|)^{1/2}$ be the governing field. This field must emphasize regions where the solution has high gradients, so that the mesh generator refines these regions.
3. Starting from the governing field φ_0 on the mesh $\mathscr{T}_0$, the anisotropic mesh generator (see [14,28]) generates a totally new mesh, denoted by $\mathscr{T}_1$.

Then, $\mathscr{T}_1$ is used to solve the problem, and so on, until the obtained solution gets clear limits between shear zones and rigid zones with no more jagged borders.

In the case of a circular section, the dissipative energy E is expressed by (11). Thus, as pointed out in the previous subsection, $\varphi = \sqrt{E}$ is continuous, but its first derivative is discontinuous, so the Hessian $H(\varphi)$ is defined with Dirac measures. From a numerical point of view, $H(\varphi)$ is not explicitly computed but rather approximated numerically. The numerical computation of $H(\varphi)$ will have high variations around the border of the plug flow. Then, the metric induced by φ will force the mesh generator to refine strongly the new mesh near this border.

This theoretical prediction can be verified in Fig. 7, which shows the initial mesh and the mesh obtained after ten loops of the adaptation process. Elements in the central plug zone become larger, while the mesh is strongly refined with stretched elements around the border of this zone and near the wall.

The same kind of properties are expected to extend to various cross-section geometries: numerical tests have confirmed that the square root of the dissipative energy appears to be a good governing field for both circular and square sections.

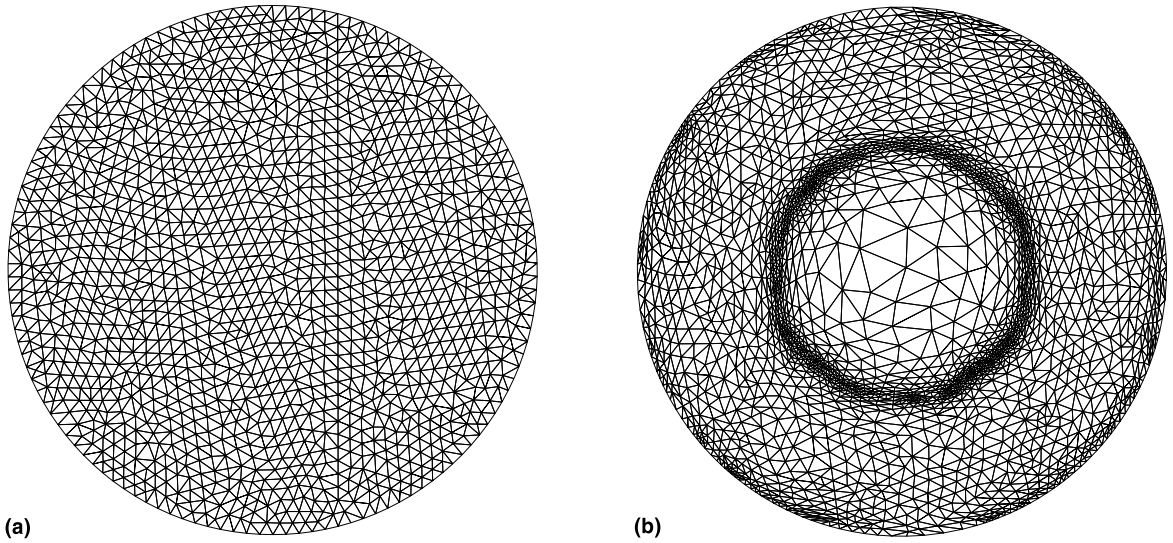

Fig. 7. Initial and adapted mesh after 10 iterations for a circular section ($Bi = 0.5$). (a) Initial uniform mesh (4000 elements); (b) adapted mesh (5000 elements).

3.5. Efficiency of the adaptation process on the square section

The influence of the mesh adaptation on the quality of our solution is shown in Fig. 8. The left column plots the adapted meshes while the right column represents the $|\boldsymbol{\sigma}_h|/\Sigma$ field for $Bi = 1$. The grey scale represents values above 1 for dark while rigid zones from 1 to 0.9 are in dark grey and in light gray for values smaller than 0.5. The $|\boldsymbol{\sigma}|/\Sigma = 1$ contour is associated with the yield surface.

The first row shows results for an isotropic regular mesh. We can see the poor accuracy of the solution, especially between shear and rigid zones, which are regions of interest. Moreover, the dead zone is unreadable.

Basing on this result, the governing field φ is computed, as described before, and then a mesh adaptation step is used. Then, the mesh plotted in the second row is obtained. This mesh is no longer regular and is slightly anisotropic. Refined regions already emphasize the shear zones. A solution to our problem can now be computed, using this mesh as a startup. The result, shown in column 2 row 2, is already better than the one computed with the initial mesh. Borders between shear and rigid zones are clearer and the dead zone in the corner has begun to be noticeable.

Going through some more cycles of adaptation loops, results are clearly improved. After 10 loops, we get the mesh and solution shown in the third row. The computational cost for 10 iterations of the adaptive process is of about one hour on an Intel/Linux (200 MHz) personal computer. The final mesh contains about 2000 triangles. Here, we have the wanted type of an anisotropic and irregular mesh. Elements are still larger in the rigid zones, both the inner plug and dead zones, while they are strongly refined in the shear zone. In particular, the regions with small element sizes are located near the wall and around the borders between shear and rigid zones. Note also that elements are stretched along these borders, as a result of the mesh anisotropy. The corresponding solution shows accurate contours and borders.

While the concavity of the separating line between shear and dead zones is turned towards the inside of the section (Fig. 8(c), right), a brutal change of concavity occurs, and concavity of contours for $|\boldsymbol{\sigma}|/\Sigma = 0.9$ turns towards corners. Thus, the prediction of dead zones requires accurate numerical computation in this region, as pointed out in Section 4.

As in the case of the circular section, the field φ is here continuous but its first derivative appears to be discontinuous. Note that in 1995, Seregin [29] showed, in a more general case, the continuity of ∇u. Fig. 9(a) represents φ in elevation in the vertical direction, for $Bi = 0.7$ and after 10 iterations of adaptation loop. One can notice that rigid zones are associated with $\varphi = 0$ and the brutal transition of φ at the separation from rigid to shear zones. The representation of both the energy field in elevation and the

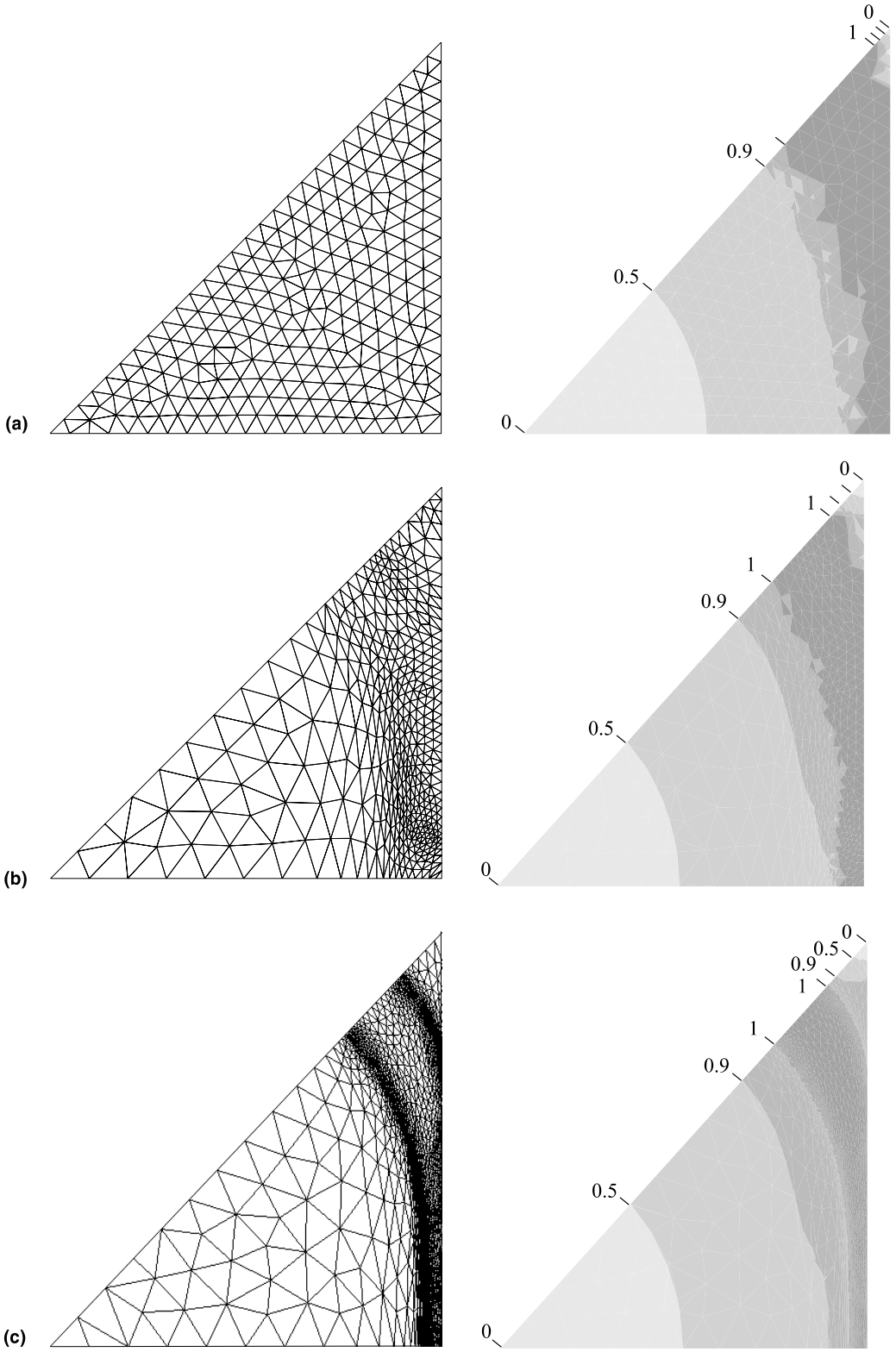

Fig. 8. Efficiency of the adaptive method: evolution of $|\sigma|/\Sigma$ during adaptation loop for $Bi = 1$. (a) Initial uniform mesh (256 vertices); (b) adapted mesh at iteration 1 (737 vertices); (c) adapted mesh at iteration 10 (1944 vertices).

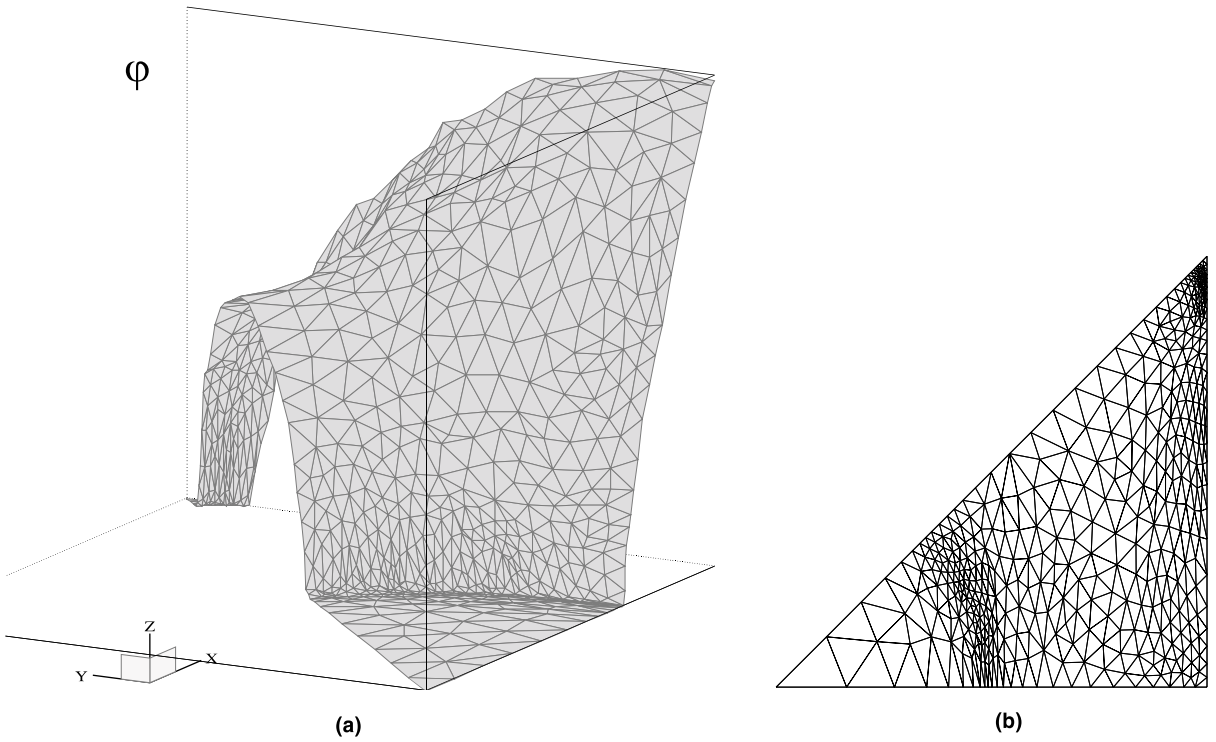

Fig. 9. (a) Elevation view of the governing field φ and the corresponding anisotropic adaptative mesh; (b) two-dimensional view of the mesh ($Bi = 0.7$, iteration 10).

corresponding anisotropic mesh shows that the mesh adapts to the surface curvature in the three dimensional space. For all computations in Section 4, 10 iterations of the adaptive process have been used.

Fig. 10 shows two successive zooms of the adapted mesh. Observe the different length scales and the anisotropy in the border of the shear zone. The first zoom shows that the mesh is able to catch in detail of the separation line between the rigid and shear zones, corresponding to $|\boldsymbol{\sigma}| = \sigma_0$. The second zoom shows also that triangles becomes flat in the direction normal to the separation line, since the adaptation is anisotropic. The shortest edge of the mesh is about 10^3 times smaller than the longest one.

4. Results on a square cross-section

4.1. Yield surfaces and velocity field

Fig. 11(a)–(c) show adapted meshes and the corresponding solutions for different Bingham numbers, namely $Bi = 0.5$, 0.9 and 1.05. Dark lines indicate the velocity contours. Let us observe the shear zone ($|\boldsymbol{\sigma}|/\Sigma \geqslant Bi$), in grey, and the two rigid zones, in white ($|\boldsymbol{\sigma}|/\Sigma < Bi$). The first rigid zone is a dead region, close to the outer corner. The second rigid zone, at the center of the flow, is an inner plug, that translates with a constant velocity in the (O_z) direction.

Let us now consider the dead region and its evolution with Bingham number. The dead region always presents a concavity turned towards the inside of the section, as pointed out in the Section 1. Note that the plug region, associated with a rigid translation movement, and the dead region, associated with zero velocity, are always separated by the shear zone, where the velocity varies gradually. Taylor and Wilson [6, Fig. 2(d), p. 98], proposed a flow with four shear zones reduced to small regions near the middle of the walls, while dead and plug regions become connected. Using the regularized model due to Papanastasiou

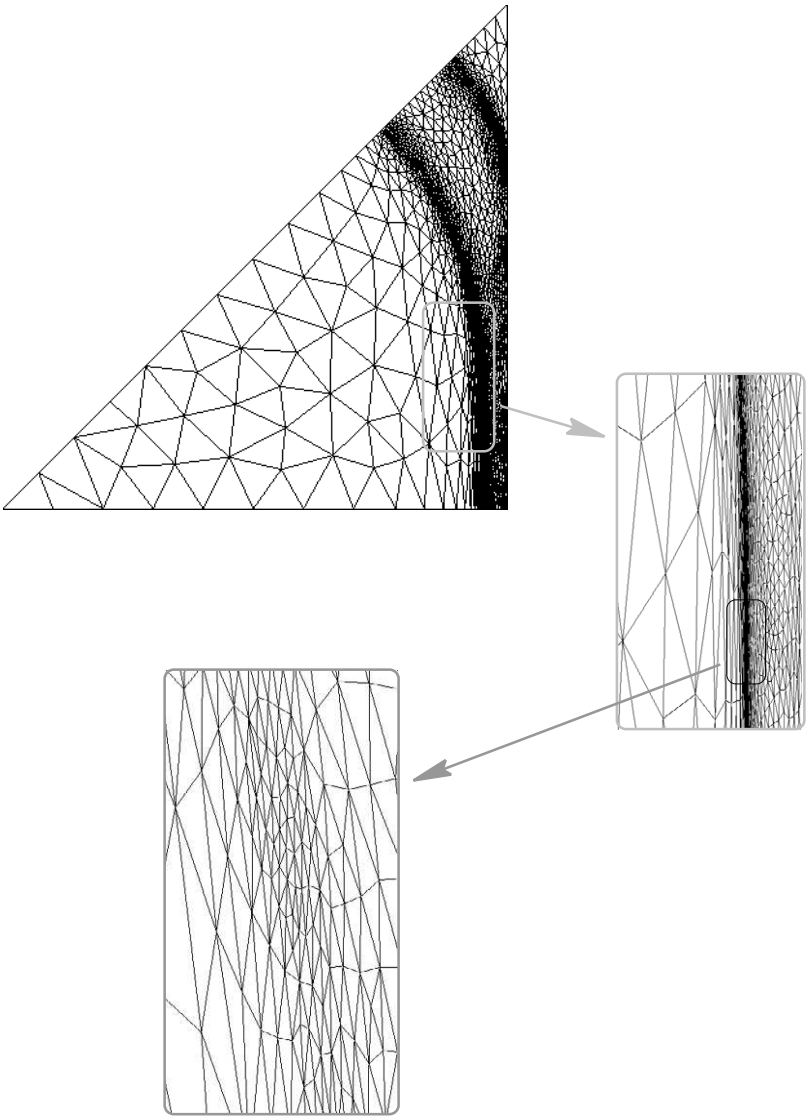

Fig. 10. Several length scales for an adapted mesh ($Bi = 1$, iteration 10).

[5], Burgos and Alexandrou [30] obtained also connected plug and dead regions (Fig. 8(d), line 1, p. 494 and Fig. 9(d), line 1, p. 495). and exhibited dead regions with inverted concavity (Fig. 8(d), line 2, p. 494). Theoretical studies showed for all $Bi > 0$ that:

1. the existence and uniqueness of the plug zone (showed by Mosolov and Mjasnikov [1]);
2. the existence of dead zones with concavity as found in the present paper (showed in 1966 by Mosolov and Mjasnikov [2]).

Our results are consistent with these properties. In particular, plug and dead zones cannot be connected before the fluid comes to a full stop. Wang [7] showed that these unexpected phenomena are due to a lack of precision in the numerical computations proposed by Taylor and Wilson [6], namely a too high value of the regularization parameter.

The inner plug is circle-like when small enough. As it grows, the inner plug gets flat due to its facing the wall. The shear zone near the middle of the wall is thinner than the one along the diagonal, but it also decreases slowly, so that the shear zone finally vanishes everywhere for the same critical Bingham number. This phenomena will be studied in detail in the following section.

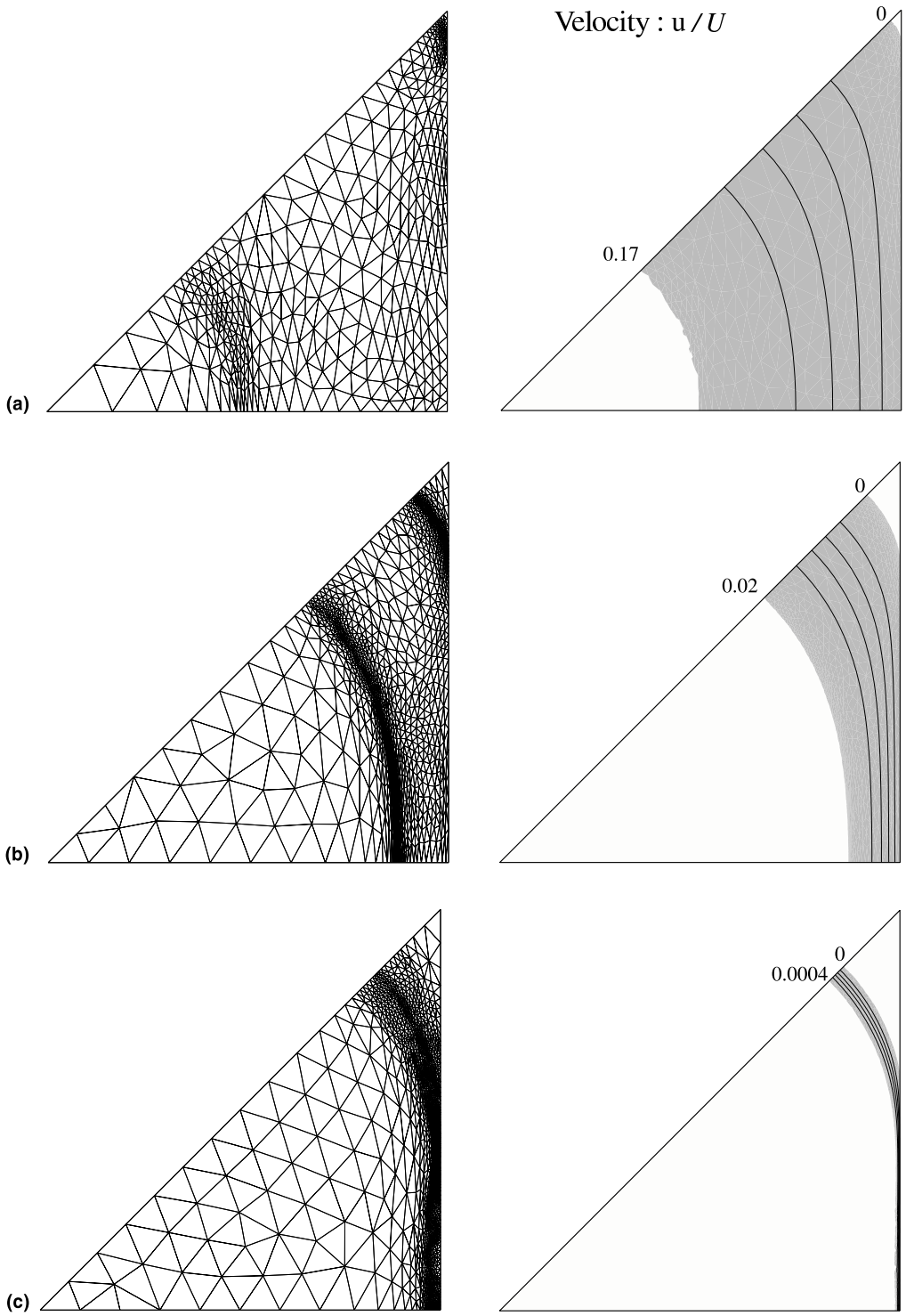

Fig. 11. Evolution versus *Bi* of velocity contours and shear (in gray) and rigid (in white). (a) $Bi = 0.5$; (b) $Bi = 0.9$; (c) $Bi = 1.05$.

The entire evolution of shear and rigid zones is described here. The fluid comes to a full stop for a Bingham number slightly greater than 1.05. For $Bi = 1.05$ (see Fig. 11(c)), an almost totally yielded cross-section appears, with only a thin shear zone. The maximum velocity, i.e velocity of the inner plug, is in this

case roughly 10^3 times smaller than the corresponding one in the Newtonian case, which is associated with a wide area of the flow.

4.2. Velocity and stress profiles

Fig. 12(a)–(d) represent the velocity u and the yield criteria $|\boldsymbol{\sigma}|/\Sigma - Bi$ profiles along the median line $x = 0$ and the diagonal line $x = y$. A curvilinear abscissa $s = \sqrt{x^2 + y^2}$ is used along the diagonal, varying from zero at the center to $\sqrt{2}L$ at the outer corner. For each cut, the evolution for several Bingham numbers, ranging from the Newtonian case ($Bi = 0$) to the full stop case is represented. Fig. 12(a) shows the growth of the inner plug region for non-zero Bingham numbers. This corresponds to the plateau that grows in size and decreases in intensity while Bi increases. The Newtonian case $Bi = 0$ is associated with a gradually varied flow. The diagonal cut of the velocity is represented on Fig. 12(b). One can observe also

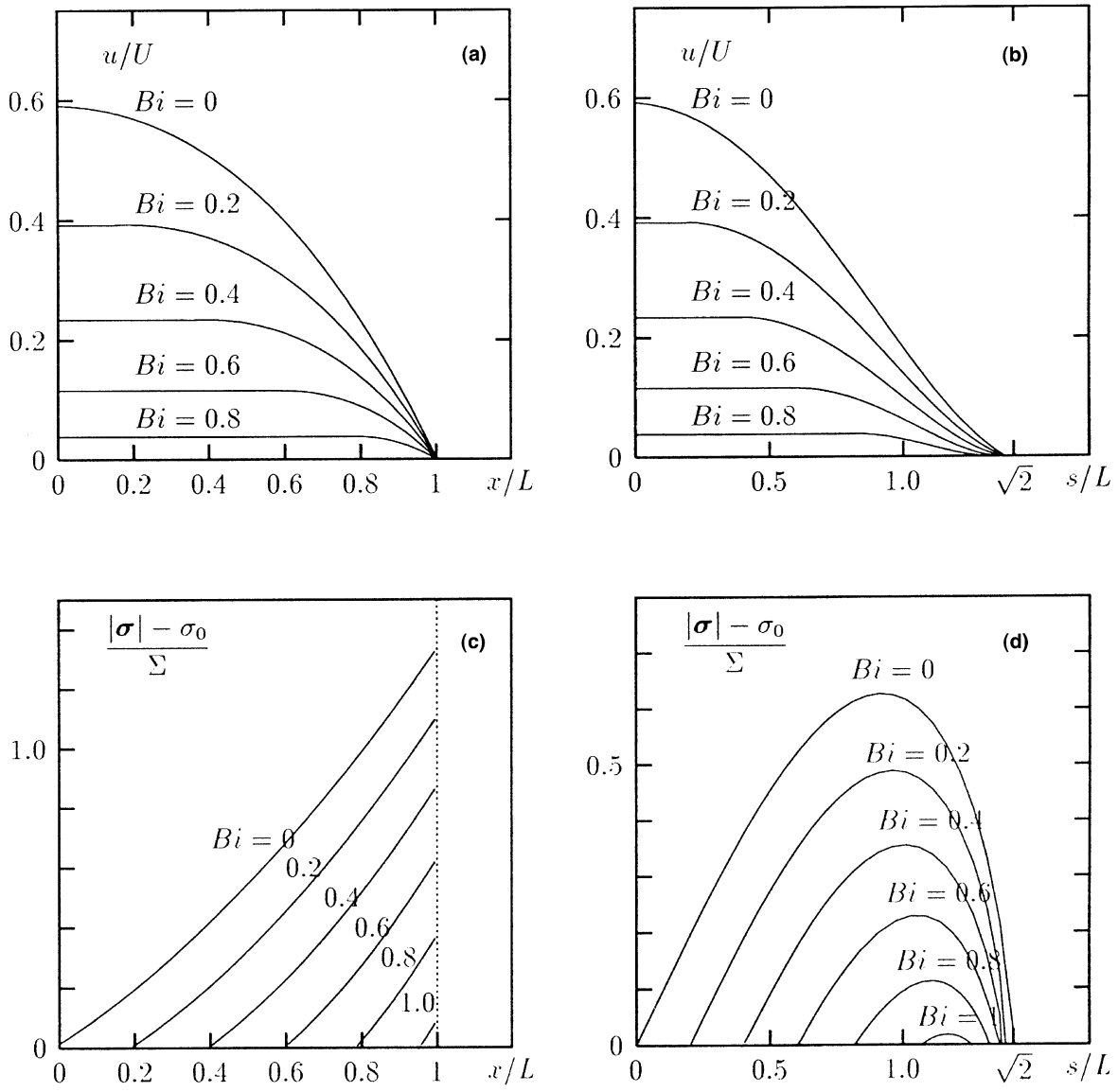

Fig. 12. Velocity profiles: (a) along the median; (b) along the diagonal; yield criteria profiles; (c) along the median; (d) along the diagonal.

the plug, represented as a plateau, and the formation of the dead region, which corresponds to curves approaching gradually the zero velocity axis as Bi increases.

Fig. 12(c)–(d) show the yield criteria. Only the positive parts of this quantity are represented, corresponding to shear zones.

In the median cut (Fig. 12(c)), one can see that the shear zone gets closer to the wall, as Bi increases. Note that the maximum value of the yield criterion over the whole section Ω is reached at the wall, i.e. along the median cut. Then, until this maximum gets to zero, there still exists a shear zone, at least at the middle of the wall, at $x = 1$. When this maximum reaches the zero value, the plug flow touches the wall, and the fluid stops.

On the diagonal cut (Fig. 12(d)), observe that the shear zone decrease, related to the expansion of both the inner plug region and the dead region. The local maximum along the diagonal cut also decreases. When this maximum reaches zero, there is no more separation between the two types of rigid zones: the plug and the dead region come into contact and the fluid stops.

4.3. Limit load analysis

The evolution described in the previous section shows that the fluid comes to a full stop for a critical Bingham number, namely Bi_c. For values of the Bingham number greater than Bi_c, the flow is totally stopped, whereas for values smaller than Bi_c it can be described by our results. When Bi increases and approaches Bi_c, the shear zone reduces to a surface, referred as the *limit yield surface*. In this section, we are interested in determining Bi_c and plotting the limit yield surface. This is done using extrapolations from data computed for several Bingham numbers, from $Bi = 0$ to $Bi = 1.05$, which is the current limit in solving the problem.

Let s_{plug} (resp. s_{dead}), as on Fig. 13(a), be the distance along the diagonal from the center of the section to the plug region border (resp. to the dead region border). Fig. 13(b) shows s_{plug} and s_{dead} as a function of the Bingham number. These distances computed numerically are interpolated by third-degree polynomials, where the coefficients are provided by a non-linear least squares fitting procedure. The intersection of the two third-order polynomial curves can also be computed, and occurs for $Bi = Bi_c \approx 1.07$ and $s_{plug} = s_{dead} \approx 1.22$ on Fig. 13(b).

By using variational methods, Mosolov and Mjasnikov [1] showed that: $Bi_c = 4/(2+\sqrt{\pi}) \approx 1.0603178\ldots$; this exact value confirms, to our point of view, the accuracy of our numerical computations.

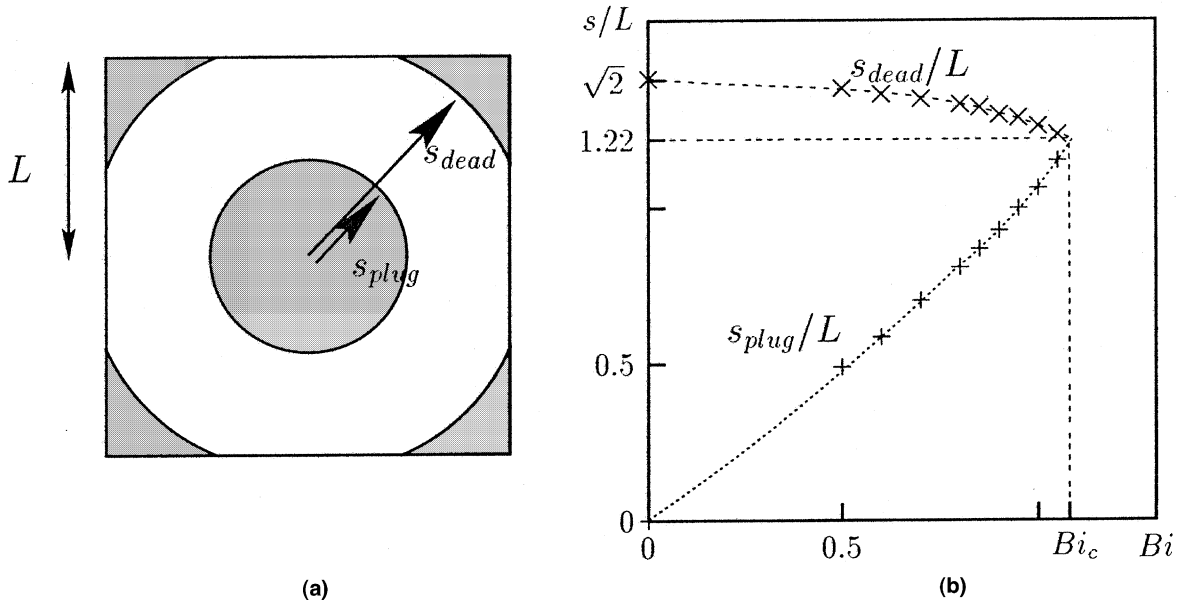

Fig. 13. Intersection of the yield surface with the diagonal: (a) schematics and notations; (b) computations and extrapolation.

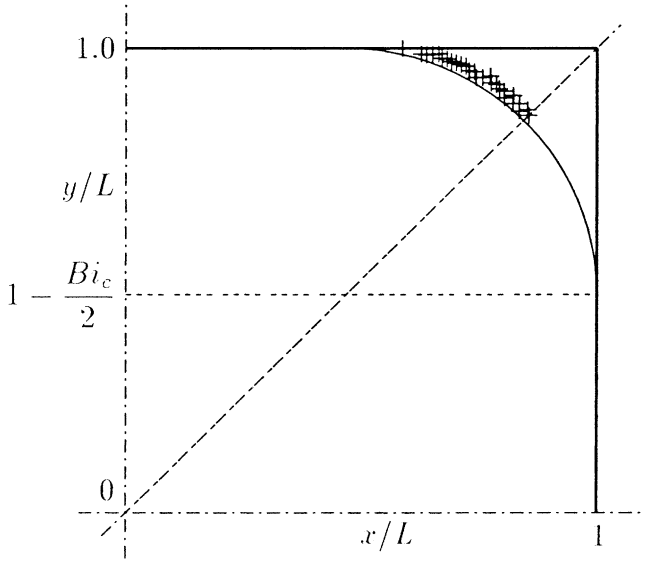

Fig. 14. The limit yield surfaces.

Taylor and Wilson [6], by using a regularized model, predicted a critical Bi_c value of 1.12. Note that these authors used another dimensionless number: $\lambda = Bi/4$ and obtained $\lambda_{crit} = 0.28$.

The previous extrapolation procedure along the diagonal is extended to other cutting directions, as shown in Fig. 14. Each cutting direction furnishes a point of the limit yield surface in the square cross-section. In Appendix A, we show that the limit yield surface is an arc of circle tangent to the wall. The radius r_c and the center (x_c, y_c) of the arc describing the limit yield surface express:

$$r_c = \frac{Bi_c}{2} \approx 0.53015890,$$
$$x_c = y_c = 1 - \frac{Bi_c}{2} \approx 0.46984110.$$

The exact yield surface is drawn in solid lines on Fig. 14, while the numerical extrapolations are represented by the + symbol. We observe that the extrapolation procedure slightly overestimates the exact coordinates. We point out that the extrapolation procedure developed here applies systematically to an arbitrary shape section while the exact yield surface can be easily explicitly expressed only for some particular section geometries (such as circle, square and rectangles).

4.4. Hydraulic analogy

This subsection aims at bringing out simple laws for use in practical designs. A classical engineering problem is to get the flow-rate as a function of the pressure drop in the pipe, given the fluid properties and the duct geometry. This result can easily be expressed by an explicit equation for a viscoplastic fluid of Bingham type, when the pipe is of a circular cross-section. Results for both circular and square pipes are compared by using the fraction $Bi/Bi_c \in [0, 1]$. This has been done for the mean velocity u_{mean}, and for the the maximum velocity u_{max}, which is the velocity of the inner plug region:

$$\frac{2\eta}{L^2 f} u_{mean}(Bi) = \frac{C_{mean}}{4}\left(1 - \frac{4}{3}\frac{Bi}{Bi_c} + \frac{1}{3}\left(\frac{Bi}{Bi_c}\right)^4\right), \tag{12}$$

$$\frac{2\eta}{L^2 f} u_{max}(Bi) = \frac{C_{max}}{2}\left(1 - \frac{Bi}{Bi_c}\right)^2, \tag{13}$$

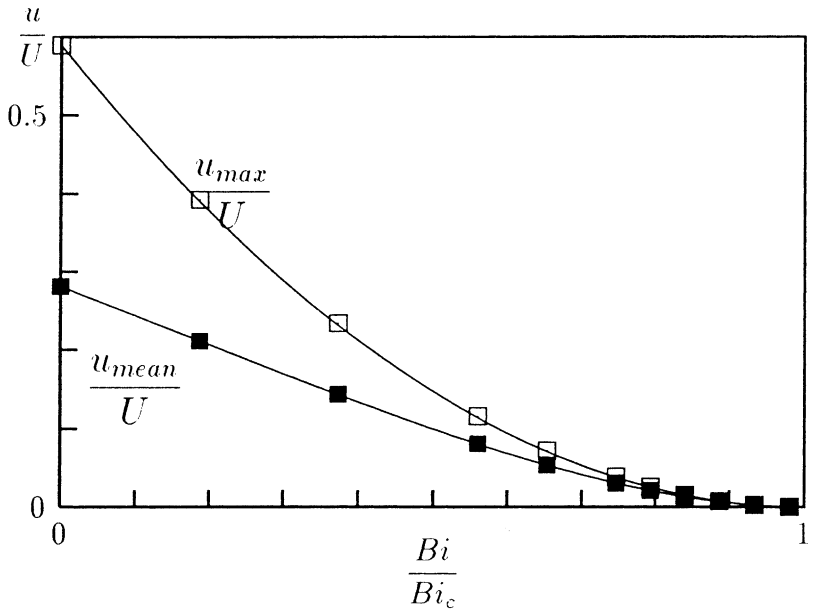

Fig. 15. Mean and maximal velocities.

where Bi is expressed by (4). The above expressions are exact for a circular section with $Bi_c = 1$ and $C_{max} = C_{mean} = 1$. In the case of a square section, Bi_c is known from the previous subsection. Moreover, C_{mean} and C_{max} can also be computed since the Newtonian solution $u(x,y)$, associated with $Bi = 0$, can be expressed using a Fourier expansions. The computation of these constants is reported in Appendix B. Fig. 15 compares u_{mean} and u_{max} as obtained by direct numerical computations in a square cross-section, and by using (12) and (13). Recall that relations (12) and (13) are not a priori exact in the case of a square cross-section. Nevertheless, the maximum of the relative error is of about 10^{-3} and cannot be seen on the plot. These relations are of practical interest for most engineering problems.

The pressure drop in a pipe of length $\mathscr{L}$ is given by $\delta p = f \times \mathscr{L}$ (see also Fig. 1(a)) and is usually compared with the kinetic energy $\rho u_{mean}^2/2$ by introducing the hydraulic coefficient Λ:

$$\delta p = \Lambda \frac{\mathscr{L}}{D_H} \frac{\rho u_{mean}^2}{2},$$

where D_H is the hydraulic diameter, defined to be four times the ratio of the section to the wetted perimeter, i.e. $D_H = 2R$ for the circular section and $D_H = 2L$ for the square section. By introducing the Reynolds number $Re = \rho u_{mean} D_H/\eta$ and using the previous expression of u_{mean}, we get:

$$\Lambda = \frac{64}{C_{mean}\, Re} \times \frac{1}{1 - \frac{4}{3}\frac{Bi}{Bi_c} + \frac{1}{3}\left(\frac{Bi}{Bi_c}\right)^4}.$$

5. Conclusion

The objective of this work is to examine the development of macroscopic features, such as flow curves and rigid zone enhancements, for the fully developed flow of a yield stress fluid in a square pipe. Our numerical resolution of the Bingham model leads to results that are qualitatively and quantitatively in good agreement with previous theoretical and numerical studies. An important result is the precision of the yield surface prediction, especially when the fluid comes close to the full stop. In that case, an extrapolation procedure leads to the limit yield surface at the full stop. Moreover, a scaling procedure extends the flow curve of a circular pipe to the case of the square pipe, interpreted as an approximate law.

The results of the present paper fully validate, to our opinion, the robustness and the accuracy of our numerical strategy. Validated on a circular cross-section and applied to a square cross-section, this approach could be applied to a tube section of any shape. Our approach combines a high order mixed finite element approximation, an anisotropic auto-adaptive mesh procedure, and the augmented Lagrangian method. The adaptive strategy allows accurate capture of the yield surfaces. This approach also eliminates the regularized parameter introduced frequently in numerical computations, and associated with a loss of accuracy.

Solving viscoplastic fluid flows in a square pipe is not only of interest as an appropriate test problem for developing the fluid mechanics of yield stress fluids, but it is also of practical interest and great importance in food and petroleum industries. In most of these cases, optimization tends to eliminate dead regions by modifying the pipe section geometry. In addition, the numerical methods used for solving this problem is of interest for various fluid and solid mechanics problems involving variational inequalities.

Appendix A. Computation of the limit yield surface and Bi_c

Mosolov and Mjasnikov [1] gave a geometric mean for the computation of Bi_c:

$$\frac{Bi_c}{2} = \sup_{\omega \subset \Omega} \frac{\mathrm{mes}(\omega)}{\mathrm{mes}(\partial\omega)}$$

they claim in [1, Lemma 2.3, p. 250], that there exists $\omega_c \subset \Omega$ such that the supremum in the previous relation is achieved. Moreover, every such ω_c satisfies the following property (Lemma 2.3, proof pp. 269–270):

> If $P \in \partial\omega_c \setminus \partial\Omega$, then the connected part of $\partial\omega_c \setminus \partial\Omega$ containing P is an arc of circle touching the wall $\partial\Omega$ and tangent to $\partial\Omega$ at the touching points.

In addition, such ω_c can be taken as the limit plug region A_c. This is obtained thanks to the Theorem 2, in [31, p. 611], that claims, in particular:

$$\frac{Bi_c}{2} = \frac{\mathrm{mes}(A_c)}{\mathrm{mes}(\partial A_c)}.$$

Hence, in the present case of a square Ω, it is established that the limit yield surface is an arc of circle tangent to $\partial\Omega$. More precisely, let us consider the subdomain $\omega(r) \subset \Omega$, obtained by replacing the corners of the square by arcs of circle of radius r and center $(1-r, 1-r)$, as shown in gray, Fig. 16. Let

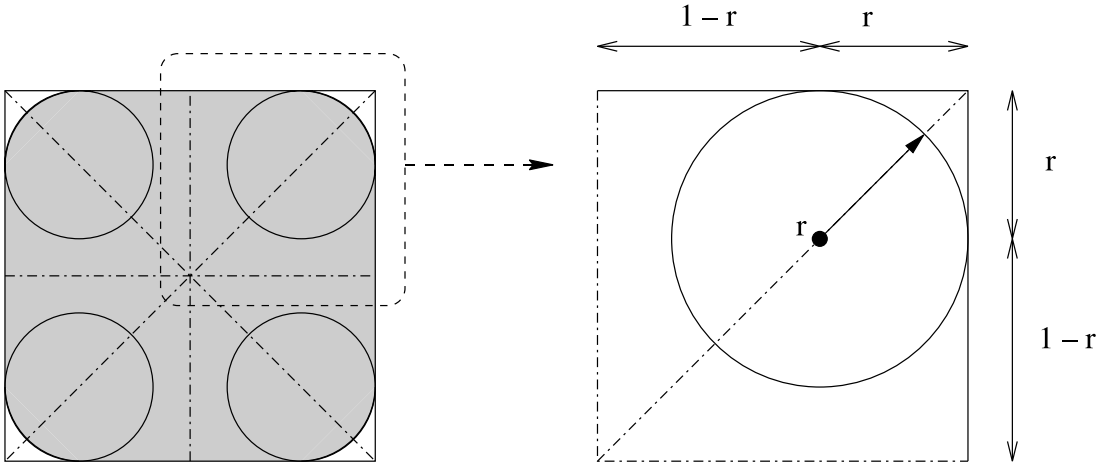

Fig. 16. Computation of Bi_c and the limit yield surface.

$$\Phi(r) = \frac{\mathrm{mes}(\omega(r))}{\mathrm{mes}(\partial\omega(r))} = \frac{(\pi-4)r^2+4}{2(\pi-4)r+8}, \quad 0 < r < 1.$$

The limit plug region A_c is an $\omega(r)$ that achieves the supremum of Φ. In particular, A_c is an $\omega(r)$ that maximize Φ. In other words, there exists $r_c \in]0,1[$ such that $A_c = \omega(r_c)$ and

$$\frac{Bi_c}{2} = \sup_{r\in]0,1[} \Phi(r) = \Phi(r_c).$$

Finally, a straightforward computation shows that

$$\frac{Bi_c}{2} = \frac{2}{2+\sqrt{\pi}} \text{ and } r_c = \frac{Bi_c}{2}.$$

Appendix B. Expression of C_{mean} and C_{max}

The solution u for $Bi = 0$ satisfies $-\Delta u = 2$ in $\Omega = [-1,1]^2$ and $u = 0$ on $\partial\Omega$. Fourier expansion leads to:

$$u(x,y) = 1 - y^2 - 4\sum_{k=0}^{\infty} \frac{(-1)^k \cosh(a_k x)\cos(a_k y)}{a_k^3 \cosh(a_k)}$$

where $a_k = (2k+1)\pi/2$. Thus, we get:

$$C_{\mathrm{mean}} = \frac{8}{3} - 16\sum_{k=0}^{\infty} \frac{\tanh(a_k)}{a_k^5} = 1.12461611964122972470774985\ldots,$$

$$C_{\mathrm{max}} = 2 - 8\sum_{k=0}^{\infty} \frac{(-1)^k}{a_k^3 \cosh(a_k)} = 1.17874165250422104902304040\ldots$$

References

[1] P.P. Mosolov, V.P. Mjasnikov, Variational methods in the theory of the fluidity of a viscous-plastic medium, PMM, J. Appl. Math. Mech. 29 (1965) 545–577.
[2] P.P. Mosolov, V.P. Mjasnikov, On stagnant flow regions of a viscous-plastic medium in pipes, PMM, J. Mech. Appl. Math. 30 (1966) 841–854.
[3] M. Bercovier, M. Engelman, A finite element method for incompressible non-newtonian flows, J. Comput. Phys. 36 (1980) 313–326.
[4] E.J. O'Donovan, R.I. Tanner, Numerical study of the Bingham squeeze film problem, J. Non-Newtonian Fluids Mech. 15 (1984) 75–83.
[5] T.C. Papanastasiou, Flow of materials with yield, J. Rheol. 31 (1987) 385–404.
[6] A.J. Taylor, D.R. Wilson, Conduit flow of an incompressible, yield-stress fluid, J. Rheol. 41 (1997) 93–101.
[7] Y. Wang, Comment on Conduit flow of an incompressible, yield-stress fluid, J. Rheol. 41 (1997) 93–101, 1387–1391.
[8] M. Fortin, Calcul numérique des écoulements des fluides de Bingham et des fluides newtoniens incompressibles par la méthode des éléments finis. thèse, Paris VI, 1972.
[9] M. Fortin, R. Glowinski, Méthodes de lagrangien augmenté. Applications à la résolution numérique de problèmes aux limites, Méthodes Mathématiques de l'Informatique, Dunod, 1982.
[10] R. Glowinski, P. Le-Tallec, Augmented Lagrangian and operator-splitting methods in nonlinear mechanics, Stud. Appl. Math., Soc. Ind. Appl. Math., 1989.
[11] R.R. Huilgol, M.P. Panizza, On the determination of the plug flow region in Bingham fluids through the application of variational inequalities, J. Non-Newtonian Fluid Mech. 58 (1995) 207–217.
[12] Y. Wang, Finite element analysis of the duct flow of Bingham plastic fluids: an application of the variational inequality, Int. J. Numer. Methods Fluids 25 (1997) 1025–1042.
[13] M.G. Vallet, Génération de maillages anisotropes adaptés. Application à la capture de couches limites, Rapport de Recherche no 1360, INRIA, 1990.
[14] H. Borouchaki, P.L. George, F. Hecht, P. Laug, E. Saltel, Delaunay mesh generation governed by metric specifications. Part I: Algorithms, Finite Elem. Anal. Des. 25 (1997) 61–83.

[15] M.J. Castro-Diaz, F. Hecht, B. Mohammadi, O. Pironneau, Anisotropic unstructured mesh adaption for flow simulations, Int. J. Numer. Methods Fluids 25 (1997) 475–491.
[16] E.C. Bingham, Fluidity and Plasticity, Mc Graw-Hill, New-York, 1922.
[17] J.G. Oldroyd. A rational formulation of the equations of plastic flow for a Bingham solid, Proc. Cambridge Philos. Soc. 43 (1947) 100–105.
[18] R.A. Adams, Sobolev Spaces, Academic Press, New York, 1975.
[19] R. Glowinski, J.L. Lions, R. Trémolières, Numerical Analysis of Variational Inequalities, North Holland, Amsterdam, 1981.
[20] I.R. Ionescu, M. Sofonea, Functional and Numerical Methods in Viscoplasticity, Oxford University Press, Oxford, 1993.
[21] F. Brezzi, M. Fortin, Mixed and Hybrid Finite Element Methods, Springer, Berlin, 1991.
[22] F. Brezzi, M. Fortin, R. Stenberg, Error analysis of mixed-interpolated elements for Reissner-Mindlin plates, Research Repport no 780, Instituto di Analisi Numerica, Pavie, 1991.
[23] P. Saramito, Numerical simulation of viscoelastic fluid flows using incompressible finite element method and a θ-method, Math. Model. Numer. Anal. 28 (1994) 1–35.
[24] P. Saramito, Efficient simulation of nonlinear viscoelastic fluid flows, J. Non-Newtonian Fluid Mech. 60 (1995) 199–223.
[25] R. Glowinski, Numerical Methods for Nonlinear Variational Problems, Springer, Berlin, 1984.
[26] R.S. Falk, B. Mercier, Error estimates for elastoplastic problems, RAIRO, série Analyse Numérique 11 (1977) 135–144.
[27] N. Roquet, R. Michel, P. Saramito, Errors estimate for a viscoplastic fluid by using P_k finite elements and adaptive meshes, C. R. Acad. Sci. Paris Sér. I 331 (7) (2000) 563–568.
[28] F. Hecht, Bidimensional anisotropic mesh generator, INRIA, 1997.
[29] G.A. Seregin, Continuity for the strain velocity tensor in two-dimensional variational problems from the theory of the Bingham fluid. Preprint 402, SFB 256 Universität Bonn, 1995.
[30] G.L. Burgos, A.N. Alexandrou, Flow development of Herschel–Bulkley fluids in a sudden three-dimensional square expansion, J. Rheol. 43 (1999) 485–498.
[31] P.P. Mosolov, V.P. Mjasnikov, On qualitative singularities of the flow of a viscous-plastic medium in pipes, J. Mech. Appl. Math. (P.M.M.) 31 (1967) 609–613.